Robotica: (2021) volume 39, pp. 1739–1759. © The Author(s), 2021. Published by Cambridge University Press.
doi:10.1017/S0263574720001472

A Parametric Study of Compliant Link Design for Safe Physical Human–Robot Interaction

Yu She†‡*, Siyang Song¶, Hai-jun Su‡ and Junmin Wang¶

†*Computer Science and Artificial Intelligence Laboratory, Massachusetts Institute of Technology, 32 Vassar St, Cambridge, MA 02139, USA*

‡*Department of Mechanical and Aerospace Engineering, Ohio State University, Columbus, OH 43210, USA*

¶*Walker Department of Mechanical Engineering, University of Texas at Austin, Austin, TX 78712, USA*

(Accepted December 25, 2020. First published online: February 3, 2021)

SUMMARY

Robots of next-generation physically interact with the world rather than be caged in a controlled area, and they need to make contact with the open-ended environment to perform their task. Compliant robot links offer intrinsic mechanical compliance for addressing the safety issue for physical human–robot interactions (pHRI). However, many important research questions are yet to be answered. For instance, how do system parameters, for example, mechanical compliance, motor torque, impact velocities, and so on, affect the impact force? how to formulate system impact dynamics of compliant robots, and how to size their geometric dimensions to maximize impact force reduction. In this paper, we present a parametric study of compliant link (CL) design for safe pHRI. We first present a theoretical model of the pHRI system that is comprised of robot dynamics, an impact contact model, and dummy head dynamics. After experimentally validating the theoretical model, we then systematically study the effects of CL parameters on the impact force in more detail. Specifically, we explore how the design and actuation parameters affect the impact force of pHRI system. Based on the parametric studies of the CL design, we propose a step-by-step process and a list of concrete guidelines for designing CL with safety constraints in pHRI. We further conduct a simulation case study to validate this design process and design guidelines.

KEYWORDS: Design; Modeling; Compliant links; Variable stiffness links; Physical human–robot interaction.

1. Introduction

In recent years, a variety of robots have been deployed or close to be deployable in an open-ended environment for numerous applications ranging from assistive devices in factory assembly lines to surgical robots to service robots for healthcare. Due to the task requirement, these robots must safely interact with human operators as well as the environment.

Physical human–robot interaction (pHRI) is one of the key components of the development of the next generation of robots. And the safety issue is one of the critical issues to be addressedfor pHRI.

* Corresponding author. E-mail: yushe@mit.edu

https://doi.org/10.1017/S0263574720001472 Published online by Cambridge University Press

An acceptable criterion is needed to evaluate the safety of the pHRI. While the head impact criterion (HIC) in ref. [1] originated from the automotive industry may be one possible choice. It suffers in ambiguities and confusions, as stated in ref. [2]. Haddadin et al.[3] conducted standardized crash tests with KUKA robots and found that the HIC and other similar criteria from the automobile industry are not appropriate to measure possible injuries for pHRI. The maximum impact force[3–5] is an alternative criterion to evaluate the results of the impact. Melvin[6] suggested the maximum allowable impact force of 660 and 4000 N, which are the fracture force of the maxilla of facial bone and frontal of the cranial bone, respectively.

Variable impedance actuators are widely employed in pHRI and similar applications involving interactions with a dynamic and unknown environment, whose main categories include active impedance by control, inherent compliance actuators, inherent damping actuators,[7] and so on. The advantage of active impedance control[8,9] is that the algorithm can adapt to both damping and stiffness modulation with an infinite range in theory. However, it suffers the drawback that it is fairly complex and requires precise dynamic models. On the other hand, the inherent damping actuator[10–13] can absorb impact energy and suppress system oscillations but requires a substantial amount of energy to accomplish highly dynamic tasks.[7] Inherent mechanical compliance is another major category for addressing the safety issue in pHRI, which can be briefly classified as joint compliance and link compliance. While extensive research has been conducted on the joint compliance,[14–27] relatively less research has been investigated for the link compliance.

Compliant link (CL) design with variable stiffness has been employed in various applications such as legged robot,[28] minimally invasive surgery,[29] and flapping-wing robot,[30] but limited applications can be found on safe pHRI. Park et al.,[31] López-Martínez et al.,[32] and Zhang et al.[33] independently developed safe link mechanisms that can switch its stiffness from high to low depending on the external collision force. The link remains a rigid part if the joint torque is below a threshold but splits into two parts if the condition is not satisfied. However, the design is bimodal, that is, the stiffness is not continuously tunable.

Stilli et al.[36] explored a stiffness controllable soft manipulator via combining pneumatic and tendon-driven actuators. Later, Stilli et al.[37] developed a variable stiffness link (VSL) made of an airtight chamber by the flexible and high-strain resistant combination of a plastic meshed silicone wall. The silicone chamber is rigid with high-pressure air but becomes soft by reducing the air pressure. She et al.[38,39] proposed an inherently safe robotic arm by designing various stiffness distribution along with the manipulator. She et al.[34,35] also proposed a continuously tunable stiffness robotic link actuated by a pair of four-bar linkages. The mechanism is able to morph the side beams, tune the cross section (hence the second moment of inertia) of the side beams, and change the lateral stiffness of the robotic link. The variable cross-section solution was supposed to offer a considerable stiffness variation ratio, but the stiffness ratio was limited due to complex boundary conditions. On the one hand, the side beams should be able to be fixed at the housings of the link to offer a stable stiffness. On the other hand, the side beams should be able to translate/rotate in the housings of the link to offer variable stiffness. The paradox resulted in challenging for the design of the connection mechanism and introduced complex boundary conditions.

These mechanisms do offer variable stiffness to address the safety of pHRI. However, how the system parameters affect the impact performance is not well studied. Furthermore, how to formulate system impact dynamics of compliant robots with CL and how to size the CL dimensions for the greatest reduction of maximum impact force remain open questions in the community.

In this paper, we conduct a comprehensive study of the effects of design and actuation parameters on the impact force during pHRI. Here, the actuation parameters are the motor torque and the initial impact velocity, while the design parameters include the link stiffness, that is, effective lateral stiffness, the end effector mass, and the ratio of the end effector mass over the robot link mass. It is worth noting that we are particularly interested in the effects of the link stiffness on the impact force since we would like to leverage variable stiffness designs to address safety issues for pHRIs. We consider robotic links whose stiffness is actively adjustable in the parametric studies in Section 5.2. Based on the parametric studies of the CL design, we then summarize a list of guidelines for designing VSLs for safe pHRI. We further provide a case study to demonstrate the feasibility of the CL design. Finally, conclusions are summarized at the end of the paper.

https://doi.org/10.1017/S0263574720001472 Published online by Cambridge University Press

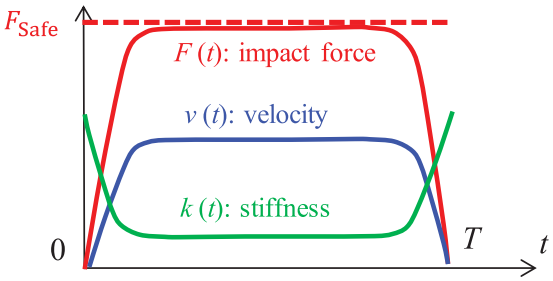


Fig. 1. A schematic view of the functioning principle of the concept of the variable stiffness arm for a typical rest-to-rest task. $v(t)$ is the robot operation speed, $k(t)$ is the robot stiffness, and $F(t)$ is the potential maximum impact force.

2. Problem Statement

In a typical rest-to-rest task, a robot generally performs as follows: (1) it increases its speed from 0 during the first stage, (2) it reaches and maintains a stable maximum speed in the second stage to maximize the time efficiency, and (3) it gradually reduces its speed to 0 and finally reaches the destination at the end of the third stage, as shown the velocity profile in Fig. 1.

The robotic link may perform an unexpected impact with a human operator and generate an impact force. We would like to make sure that the potential impact force is lower than a safety threshold (F_{safe}) to ensure inherent safety while achieving the time efficiency as high as possible. High operation speeds of the manipulator are desired from the perspective of time efficiency, and high safety is required for pHRIs.

Let us consider a traditional robotic manipulator with constant stiffness or constant stiffness link (CSL). To keep the impact force lower than the F_{safe}, one may consider keeping the robot operation speeds lower than a critical value, but it will reduce the robot's performance (not time-efficient). On the other hand, high robot operation speeds attain time efficiency but may cause severe injuries (large impact force). High performance (e.g., time efficiency) and high safety are challenging to be simultaneously achieved for traditional robots with constant stiffness. However, this problem may be solved by utilizing a VSL.

The potential impact force is determined by impact velocity, robot stiffness, and mass involved in the impact (including robot effective mass and object effective mass).[54] Given a particular manipulation task, the mass of the objects is generally fixed, and we do not have control over it. Here, we consider the effect of the impact velocity $v(t)$ and robot stiffness $k(t)$ on the impact force $F(t)$.

Now let us consider a robotic arm whose stiffness is actively tunable. One can tune down the robot stiffness during fast motion such that the robot is time-efficient while keeping high safety. Similarly, when the robot runs slow for position control or force control, one can tune up the robot stiffness to improve its performance (e.g., accuracy and resolution). In this way, the variable stiffness arm provides a potential solution to simultaneously achieve high safety and high performance (e.g., time efficiency, high accuracy, and high resolution). A schematic view of robot operation velocity $v(t)$, the robot stiffness $k(t)$, and the potential impact force $F(t)$ are shown in Fig. 1.

Intuitively, a stiffer link produces a larger maximum impact force. Assume the VSL has a stiffness range of $[k_1, k_2]$, as shown in Fig. 2(a). The corresponding maximum impact force is $[F_1, F_2]$. Giving a VSL, one can reduce the robot stiffness (Δk) to lower the potential maximum impact force (ΔF).

Next, we would like to compare the CSL and VSL in terms of the maximum impact force. Assume the CSL has a stiffness of k_2. For the CSL, one can find the maximum operation speed of the CSL is v_1 for safe pHRIs, given the critical impact force F_{safe}, as shown in Fig. 2(b). v_1 is the critical operation speed for the CSL. If the CSL operation speed increases from v_1 to v_2, as shown in Fig. 2(b), the maximum impact force will increase from F_1 to F_2 accordingly. Note, $F_2 > F_{\text{safe}}$, which can result in irreversible damages for the human operator.

For the VSL whose stiffness is in the range of $[k_1, k_2]$, it's stiffness can be actively tuned down from k_2 to k_1 when the robot operation speed increases from v_1 to v_2. In this way, the maximum

https://doi.org/10.1017/S0263574720001472 Published online by Cambridge University Press

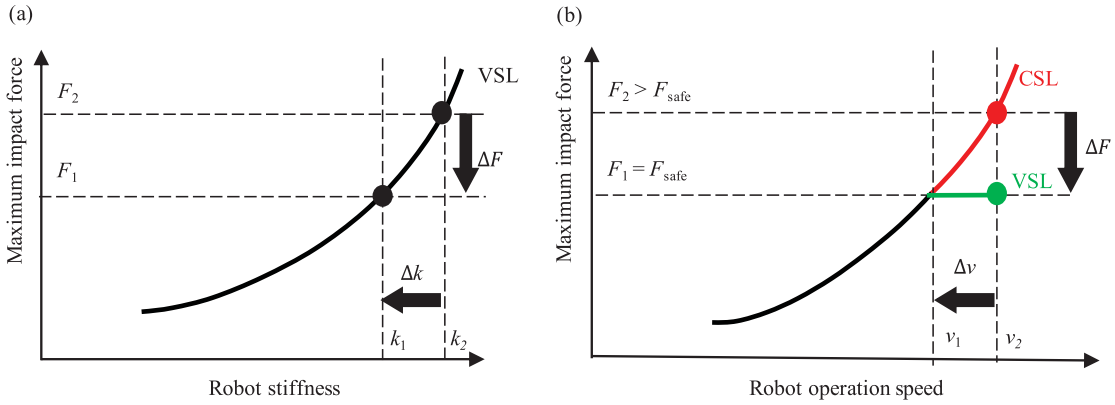


Fig. 2. A schematic view of (a) maximum impact force versus robot stiffness and (b) maximum impact force versus robot operation speed. CSL and VSL represent constant stiffness link and variable stiffness link, respectively.

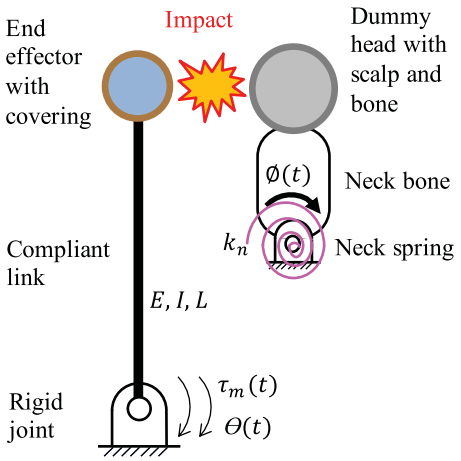


Fig. 3. A physical human–robot interaction system is comprised of a dummy head and a compliant link with a rigid joint.

impact force generated by the VSL will remain as F_{safe}. Therefore, the VSL remains safe for pHRIs at a high operation speed of v_2.

The VSL is able to run faster than the CSL while guaranteeing inherently safety. Therefore, the VSL design offers a more time-efficient solution. The core idea here is to leverage the robot stiffness reduction, instead of the robot speed reduction (the traditional method), to achieve impact force reduction. In this way, one can simultaneously obtain high safety and high time efficiency. Now the questions become where is the effective range of the stiffness variation and how to design such a VSL. These questions will be detailed in the rest of this paper.

3. System Modeling

The robot of a pHRI system is comprised of a rigid body pin joint, a CL, and the end effector, as shown on the left of Fig. 3. The CL has Young's modulus E, a length L, the second moment of inertia I, and a mass m_r. And the human head is modeled with a dummy head covered with soft scalp and a rigid necked bone connected to the ground via a torsion spring k_n, as shown in the right part of Fig. 3. Similar to the techniques presented in ref. [45], we apply Lagrange equations to model the dynamics of the robot/head and treated the unexpected impact with an external force. While the Ogden model is implemented in ref. [45] to model the nonlinearity of the contact force, we applied the piecewise Hertz contact model[41] in this study to simulate the impact force.

https://doi.org/10.1017/S0263574720001472 Published online by Cambridge University Press

3.1. The dynamics model of the pHRI system

The dynamics of the pHRI system with a CL include CL dynamics and dummy head dynamics. Here, we model the CL using the assumed modes method (AMM[49,50]). Then, the dynamics of the pHRI system with link compliance on the robot can be described as follows:

$$\begin{cases} \mathbf{M}(\mathbf{q})\ddot{\mathbf{q}} + \mathbf{N}(\mathbf{q}, \dot{\mathbf{q}}) + \mathbf{D}(\mathbf{q})\dot{\mathbf{q}} + \mathbf{G}(\mathbf{q}) + \mathbf{K}\mathbf{q} = \boldsymbol{\tau} + \boldsymbol{\tau}_{\text{er}} \\ I_h\ddot{\phi} + g_h(\phi) = \tau_h + \tau_{\text{eh}}, \end{cases} \tag{1}$$

where $\mathbf{M}(\mathbf{q})$ is the inertia matrix, $\mathbf{N}(\mathbf{q}, \dot{\mathbf{q}})$ contains the centrifugal and nonlinear Coriolis terms, $\mathbf{D}(\mathbf{q})$ is the damping matrix,[51,52] $\mathbf{G}(\mathbf{q})$ is the gravity matrix, and $\mathbf{K}$ is the stiffness matrix. Considering the first two modes of the AMM, the generalized coordinates are $\mathbf{q} = [\theta, a_1, a_2]^T$, from which θ is the motor angle and a_1 and a_2 are modal coordinates. τ_h and τ_{eh} are the spring torque and external torque of the dummy head, which can be calculated as follows:

$$\begin{cases} \tau_h = k_h\phi \\ \tau_{\text{eh}} = J_h^T f_e(\delta) \end{cases} \tag{2}$$

where ϕ represents the deformation angle of the neck, given an impact from the impactor to the dummy head; k_h is the neck stiffness; J_h is the Jacobian of the neck bone and is equal to l in this case; δ and $f_e(\delta)$ are the penetration depth and contact force, which will be detailed in Section 3.2. Given the vibration mode functions of $\varphi_1(x)$ and $\varphi_2(x)$, from which x is the position of an arbitrary point on the CL from the perspective of the floating frame, we have

$$\begin{cases} \boldsymbol{\tau} = [\tau_m, 0, 0]^T \\ \boldsymbol{\tau}_{\text{er}} = \mathbf{J}_{\text{cl}}^T \mathbf{F}_e(\delta) - \boldsymbol{\tau}_f \\ \mathbf{J}_{\text{cl}} = \begin{bmatrix} J_{11} & -\varphi_1(L)\sin\theta & -\varphi_2(L)\sin\theta \\ J_{21} & \varphi_1(L)\cos\theta & \varphi_2(L)\cos\theta \end{bmatrix} \\ J_{11} = -L\sin\theta - (\varphi_1(L)a_1(t) + \varphi_2(L)a_2(t))\cos\theta \\ J_{21} = L\cos\theta - (\varphi_1(L)a_1(t) + \varphi_2(L)a_2(t))\sin\theta, \\ \mathbf{F}_e(\delta) = [-f_e(\delta), 0]^T \\ \boldsymbol{\tau}_f = [\tau_f, 0, 0]^T \end{cases} \tag{3}$$

where τ_m is the motor torque, τ_f is the friction torque,[53] $\mathbf{J}_{\text{cl}}$ is the Jacobian of the robot with CL that is calculated based on AMM, and f_e is the contact force between the robot and the dummy head, assuming an impact occurs between them.

3.2. The Hertz contact model

The linear mass-spring-mass model is widely used to model the contact force of a robot–human impact system in literature[2,3,17] owing to it is simplicity. The simplified linear contact model offers the benefits of explicit expressions of the impact force, but it cannot address the contact nonlinearity from the material and geometry properties on the contacting surface. On the contrary, Hertz contact model[40,41,46] considers the geometric and material characteristics and is more accurate to model the contact, which is considered in this study. The piecewise Hertz contact model[41] is implemented in this study, considering the biomechanical structure of the human head (material properties of scalp and skull are significantly different). Assume the impact occurred between an impactor and the dummy head. The impactor is installed at the tip of a robot link, while the dummy head is fixed at the end of a neck bone. The impactor is comprised of an end effector with covering material, as shown at the left bottom of Fig. 4, and the dummy head is comprised of a scalp covering a skull bone as shown at right bottom. In this work, the impactor is made of an aluminum base covered with soft material (polydimethylsiloxane/PDMS), while the head mass is simulated by an aluminum block, and the scalp is represented by a silicone rubber surface (Silicone Max 20), respectively.

https://doi.org/10.1017/S0263574720001472 Published online by Cambridge University Press

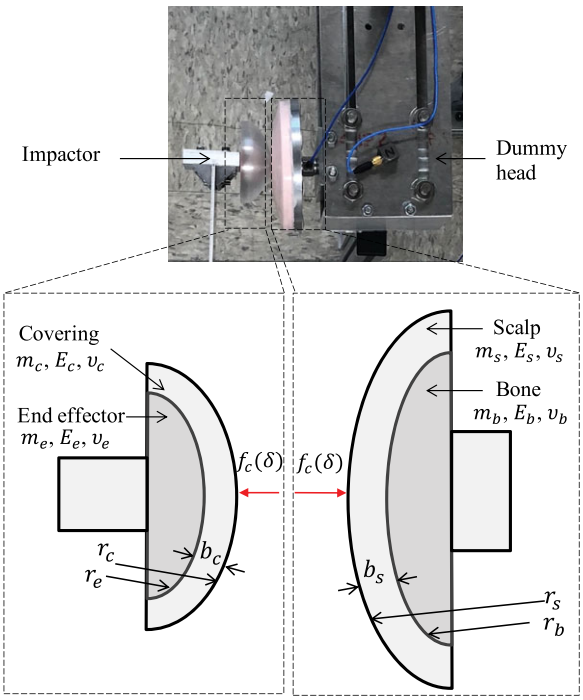


Fig. 4. The schematic and physical setting of the impact system.

Assuming the materials of the contact bodies are isotropic, homogeneous, and frictionless, the piecewise Hertz contact model is employed and the contact force can be calculated as follows:

$$f_e(\delta) = \begin{cases} k_{\text{cs}}\delta^{n_{\text{cs}}}, \ \delta \le b_{\text{sm}} \\ k_{\text{cb}}(\delta - b_{\text{sm}})^{n_{\text{cb}}} + f_e(b_{\text{sm}}), \ b_{\text{sm}} < \delta \le b_{\text{cm}} \\ k_{\text{eb}}(\delta - b_{\text{cm}})^{n_{\text{eb}}} + f_e(b_{\text{cm}}), \ b_{\text{cm}} \le \delta, \end{cases} \tag{4}$$

where $f_e(\delta)$ is the contact force and δ is the penetration depth. The Hertz exponents n_{cs}, n_{cb}, and n_{eb} are determined based on the contact materials. b_{cm} and b_{sm} are the maximum compression depths of the covering and scalp. According to ref. [42], a soft material is considered fully compressed given the penetration depth exceeding 80% of the thickness of the soft material. k_{cs}, k_{cb}, and k_{eb} are stiffness constants between covering and scalp, covering and bone, and end effector and bone, respectively, which can be calculated as follows:

$$\begin{cases} k_{\text{cs}} = \dfrac{4}{3}\left(\dfrac{1-\nu_c^2}{E_c} + \dfrac{1-\nu_s^2}{E_s}\right)^{-1}\left(\dfrac{1}{R_c} + \dfrac{1}{R_s}\right)^{-\frac{1}{2}} \\ k_{\text{cb}} = \dfrac{4}{3}\left(\dfrac{1-\nu_c^2}{E_c} + \dfrac{1-\nu_b^2}{E_b}\right)^{-1}\left(\dfrac{1}{R_c} + \dfrac{1}{R_b}\right)^{-\frac{1}{2}} \\ k_{\text{eb}} = \dfrac{4}{3}\left(\dfrac{1-\nu_e^2}{E_e} + \dfrac{1-\nu_b^2}{E_b}\right)^{-1}\left(\dfrac{1}{R_e} + \dfrac{1}{R_b}\right)^{-\frac{1}{2}}. \end{cases} \tag{5}$$

where E, ν, and R represent Young's modulus, Poisson ratio, and geometric radius, and subscripts c, s, e, and b represent the covering material, scalp, end effector, and bone, respectively.

The definitions of the parameters of the Hertz contact model in Eqs. (4) and (5) are given in Table I. These parameters are referred to ref. [41] for the simulation purpose, except some geometric parameters (R_b and R_c) which are not given in ref. [41]. They are determined according to the materials implemented in our experimental setup.

With the parameters in Table I, one can obtain the relationship between the impact force and penetration depth as shown in Fig. 5. It is observed that the impact force exponentially increases

https://doi.org/10.1017/S0263574720001472 Published online by Cambridge University Press

Table I. The Hertz contact model parameters.

Parameters (units)	**Symbol**	**Value**
Bone Young's modulus (N/m^2)	E_b	6.5E9
Bone mass (kg)	m_b	4.5
Bone radius (m)	R_b	0.0845
Bone Poisson ratio	ν_b	0.22
Covering material Young's modulus (N/m^2)	E_c	70E6
Covering material mass (kg)	m_c	0.11
Covering material radius (m)	R_c	0.034
Covering material thickness (m)	b_c	0.02
Covering material Poisson ratio	ν_c	0.25
End effector Young's modulus (N/m^2)	E_e	70E9
End effector mass (kg)	m_e	1
End effector radius (m)	R_e	0.03
End effector Poisson ratio	ν_e	0.3
Hertz exponent (covering-scalp)	n_{cs}	1.65
Hertz exponent (covering-bone)	n_{cb}	1.8
Hertz exponent (effector-bone)	n_{eb}	2.65
Scalp Young's modulus (N/m^2)	E_s	16.7E6
Scalp mass (kg)	m_s	0.042
Scalp radius (m)	R_s	0.0875
Scalp thickness (m)	b_s	0.003
Scalp Poisson ratio	ν_s	0.42
Stiffness (covering-scalp) (Pa.m$^{1/2}$)	k_{cs}	3.327E6
Stiffness (covering-bone) (Pa.m$^{1/2}$)	k_{cb}	1.533E7
Stiffness (effector-bone) (Pa.m$^{1/2}$)	k_{eb}	7.91E8

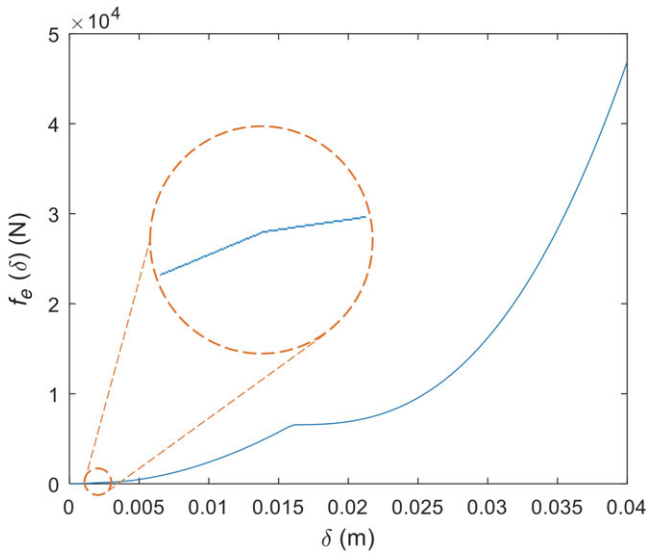


Fig. 5. The impact force f_e versus penetration depth δ.

with respect to the increasing of the penetration depth. In addition, there are three segments of the impact force penetration profile, since there are three contact situations, including covering-scalp, covering-bone, and effector-bone.

We implemented the above theoretical model in Matlab codes. It takes approximately 0.45 s on a laptop (Intel®Core™ i7 CPU 2.4 GHz) to execute a single impact simulation with the dynamics of the pHRI system with a CL. The high efficiency of the dynamic model solver allows us to conduct massive simulations for parametric studies and various design case studies in the following sections.

https://doi.org/10.1017/S0263574720001472 Published online by Cambridge University Press

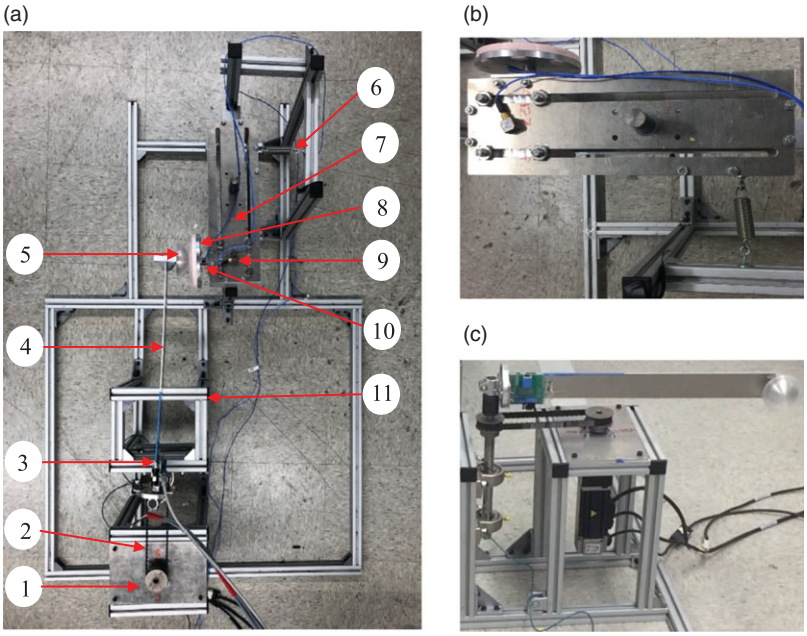


Fig. 6. (a) The experiment setup, (b) the physical model of the dummy head, and (c) the front view of the compliant link with the actuator. (1) The motor and gearbox with the support frame, (2) the pulley to protect the motor from impact, (3) the strain gauges installed at the root of the robot link, (4) the compliant mode robot link, (5) the impactor fixed at the end of the link, (6) the neck spring, (7) the neck bone, (8) the dummy head, (9) the acceleration sensor, (10) the force sensor, and (11) the overall frame of the whole pHRI system.

4. Experimental Validation of Models

To validate the theoretical model derived above, we established an experimental platform based on the configuration in Fig. 3. We compared the impact force profile of the theoretical model against experimental results.

4.1. Experiment setup

Figure 6 shows the experimental setup of the pHRI system. Figure 6(a) shows various components of the experiment setup. Figure 6(b) details the dummy head, which is also shown at the top part of Fig. 4. And Fig. 6(c) shows the front view of the CL with the actuator. The actual experimental parameters are given in Table II.

The design of the experimental setup is detailed in the following. A servo motor[1] and its associated driver[2] are installed on the aluminum platform frame. A gearbox[3] is installed at the output shaft of the motor to reduce the speed and increase the motor torque. A timing belt with a set of pulleys is used to connect the output shaft of the gearbox and the rotational shaft of the robot link to protect the motor from the physical impact between the robot and the dummy head. Note, the belt-associated pully is adjustable. We first manually tight the belt as much as we can, then we fix the movable pulley. We apply a lateral force at the tip of the flexible beam and observe considerable deformations (5% of the beam deformation over the beam length) of the flexible beam without obvious movements of the belt. In this way, the physical configuration ensures the compliance from the timing belt is neglectable comparing with the compliance from the flexible beam. Given the relatively low impact velocity studied in this experiment (the impact velocity is less than 1 m/s), we assume that the observation under the quasi-static condition applies to the transient dynamic impact as well.

[1]Model J0400-351-4-000, Applied Motion.

[2]Model SV2A5-Q-AE, Applied Motion.

[3]Model 23PL070, Applied Motion.

https://doi.org/10.1017/S0263574720001472 Published online by Cambridge University Press

Table II. Experimental parameters of the pHRI system.

Parameters (units)	Value	Parameters (units)	Value
b_c (m)	0.01	b_s (m)	0.003
E_b (N/m^2)	71E9	E_c (N/m^2)	2.61E6
E_r (N/m^2)	71E9	E_s (N/m^2)	0.84E6
I_m (kg.m^2)	3.26E-5	k_h (N.m/rad)	1
k_l (N/m)	111.0522	L (m)	0.58
l (m)	0.147	m_b (kg)	2
m_e (kg)	0.127	m_n (kg)	2
m_r (kg)	0.21	n_{cb}	1.2
n_{cs}	1.12	n_{rb}	2.65
R_b (m)	0.0845	R_c (m)	0.045
R_r (m)	0.035	R_s (m)	0.0875
v_0 (m/s)	[0.5,1]	ν_b	0.3
ν_c	0.278	ν_r	0.3
ν_s	0.5	τ_m (N.m)	0

A set of full-bridge strain gauges are attached at the root of the robot link to measure the lateral deflection. A force sensor[4] (sensitivity: 5 mV/lb) and an acceleration sensor[5] (sensitivity: 10 mV/g) are used to monitor the impact results. The sensor data are measured by a signal conditioner.[6] An embedded controller[7] is used for the control and data acquisition in this testing (not shown).

It is worth mentioning that the robot operation speeds for pHRIs are relatively low in this work, and the link deformation is small and simple. The first-order vibration mode dominates the beam deflection after an impact. The strain gauges applied in this study work for simple deformations. For other applications with high speeds and complex deformations (high-order vibration modes), one may consider other feedback solutions such as high-speed cameras.

The servo motor is able to provide a constant velocity by a simple model-based controller. Once an impact occurs, the force sensor detects the impact, and the motor torque is cut off immediately for simulating the free impact. It is worth noting that the sample rate of the digital controller is 2000 Hz and the control action has around 0.5 ms delay after the detection of an impact event. The maximum impact velocity is limited to 1.0 m/s during the test in order to protect the servo motor. We tried the impact velocities of 0.5, 0.75, and 1.0 m/s, and each velocity was repeated five times. The impact force has multiple waves, and the first one has the largest peak value, which is the focus of this study.

It is worth noting that n_{cs}, n_{cb}, and n_{rb} are determined from an independently experimental testing data to ensure the theoretical model agrees with the experiment data given $v_0 = 0.75$ m/s. The method to find n_{cs}, n_{cb}, and n_{rb} for static compression test can refer to our previous work.[43] However, this study analyzes the transient impact force instead of static compression force in ref. [43]. It is identified that $n_{\text{cs}} = 1.12$, $n_{\text{cb}} = 1.2$, and $n_{\text{rb}} = 2.65$ give the minimal accumulated errors (averaged) between the results from the theoretical model and the separate testing data. We then fixed these parameters for the theoretical model.

4.2. Testing results

Figure 7 shows the impact force from the theoretical model and testing results. Note, we aligned the start point of the impact from the experiment with that from the model for the sake of comparison. The theoretical model can basically agree with the testing data with relatively large variation. The average errors between the theoretical results and the experiment data during the impact interval are 9.23%, 9.76%, and 19.16% with respect to the impact velocity of 0.5, 0.75, and 1.0 m/s, respectively. It is observed that the theoretical model can be more accurate when v_0 is relatively small. Note, the force sensor has a measurement range of 4.448 kN under compression with a high resolution of

[4]Model 208C04, PCB Piezotronics.

[5]Model 352C03, PCB Piezotronics.

[6]Model 482C05, PCB Piezotronics.

[7]Model CompactRIO 9035, National Instruments.

https://doi.org/10.1017/S0263574720001472 Published online by Cambridge University Press

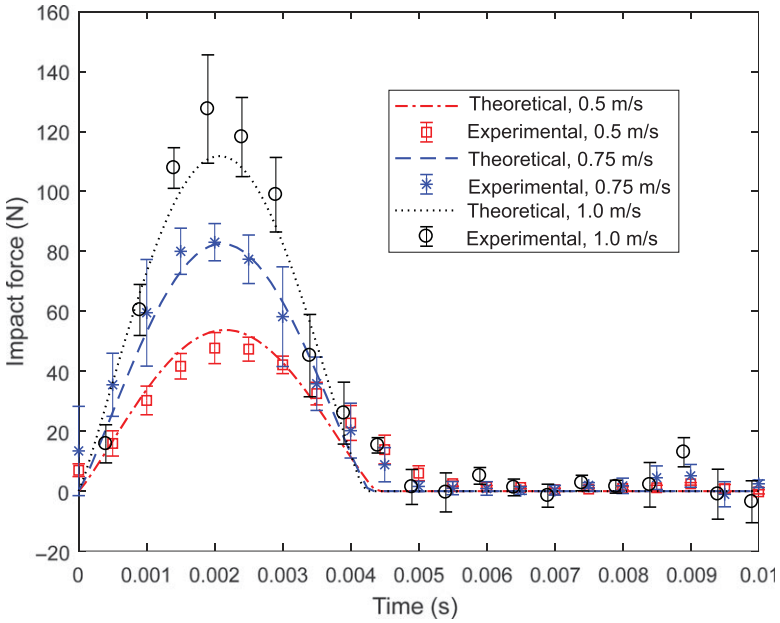


Fig. 7. The impact force from the testing results and theoretical simulation.

0.04448 N-rms. One of the potential reasons for the variances between the experiment results and the model data can be from the delay of the control action after the impact detection. Furthermore, the nature of the complex pHRI system (including robot dynamics, impact model, and head dynamics) brings challenges to formulate a precise system model. For instance, although the piecewise Hertz contact model considers the different physical properties of the contact objects (bones and skins), it does not consider the viscous term of the material. In addition, the Hertz contact model considers the normal impact force but does not take the shear force into consideration. These factors potentially contribute to the relatively large errors between the experiment data and the model.

5. Parametric Studies

After validating the theoretical model, we study the effects of the design parameters and actuation parameters on the impact force in this section.

Recall, the actuation parameters include the motor torque τ_m and the initial impact velocity v_0, and the design parameters are the link stiffness k_l, end effector mass m_e, and mass ratio R_m which is defined as:

$$R_m = \frac{m_r}{m_e}, \tag{6}$$

where m_r and m_e are the mass of the robot arm and end effector respectively. Note, here we consider the covering material is much lighter than that of the end effector, and m_e dominates the mass of the impactor. Specifically, we will study the general effects of those parameters and their effects under variable stiffness.

5.1. General effects

Based on the system model, we can run extensive simulations with varying both design and actuation parameters. And then we analyze the simulation data and conduct parameter sensitivity studies. Figure 8 shows the effects of the design parameters (k_l, R_m, and m_e) on the impact force. The parameters of the contact model are given in Table I and the rest of the parameters of the pHRI system are given in Fig. 8.

5.1.1. Effect of design parameters on the impact force. First, we study the effects of lateral stiffness k_l on the impact force. The physical parameters of the contact model are partially from ref. [41] and the rest parameters of the pHRI system are given in Table I. Here, the motor torque is set to be zero

https://doi.org/10.1017/S0263574720001472 Published online by Cambridge University Press

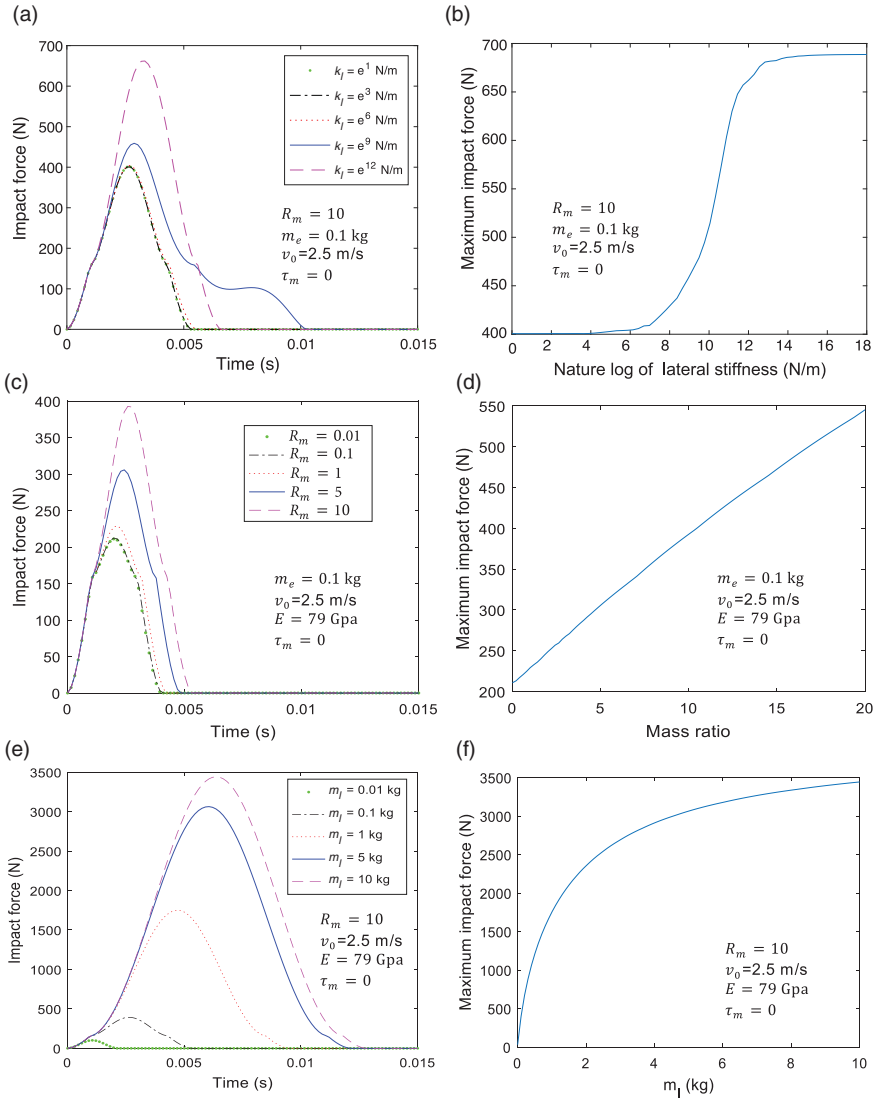


Fig. 8. The effects of various parameters of the CL design on the impact force. (a) The impact force versus time given $R_m = 10$, $m_e = 0.1$ kg, $v_0 = 2.5$ m/s, $\tau_m = 0$, and various lateral stiffnesses; (b) the maximum impact force versus lateral stiffness given $R_m = 10$, $m_e = 0.1$ kg, $v_0 = 2.5$ m/s, $\tau_m = 0$; (c) the impact force versus time given $m_e = 0.1$ kg, $v_0 = 2.5$ m/s, $E = 79$ GPa, $\tau_m = 0$, and various mass ratio; (d) the maximum impact force versus mass ratios given $m_e = 0.1$ kg, $v_0 = 2.5$ m/s, $E = 79$ GPa, $\tau_m = 0$; (e) the impact force versus time given $R_m = 10$, $v_0 = 2.5$ m/s, $E = 79$ GPa, $\tau_m = 0$, and various end effector mass; and (f) the maximum impact force versus end effector mass given $R_m = 10$, $v_0 = 2.5$ m/s, $E = 79$ GPa, $\tau_m = 0$.

(passive impact), and the impact velocity is set to be $v_0 = 2.5$ m/s. Notably, considering the safety criterion discussed in Section 1, the impact velocity here is set relatively high such that the impact force is sufficiently large to evaluate the effectiveness of the various parameters as suggested by ref. [6]. By varying k_l, we plot the impact force versus time, as shown in Fig. 8(a). Here, e is the base of the natural logarithm (i.e., $e \approx 2.72$).

If a continuous and wide range of k_l is given and only the peak of the impact force is considered, one can plot the maximum impact force $F_{\max}(k_l)$ in Fig. 8(b). Please note, we take a natural logarithm operation of the actual lateral stiffnes in the x-axis in Fig. 8(b) in order to see a clear trend of the stiffness variation. Here, $F_{\max}$ is captured from the maximum value of each batch of simulation results. Figure 8(c) plots the impact force versus time given different mass ratios R_m, and Fig. 8(d) shows the maximum impact force $F_{\max}$ given a continuous and wide range of mass ratios R_m. Figure 8(e) and (f) present the effects of m_e on the impact force. According to this figure, we had the following observations:

https://doi.org/10.1017/S0263574720001472 Published online by Cambridge University Press

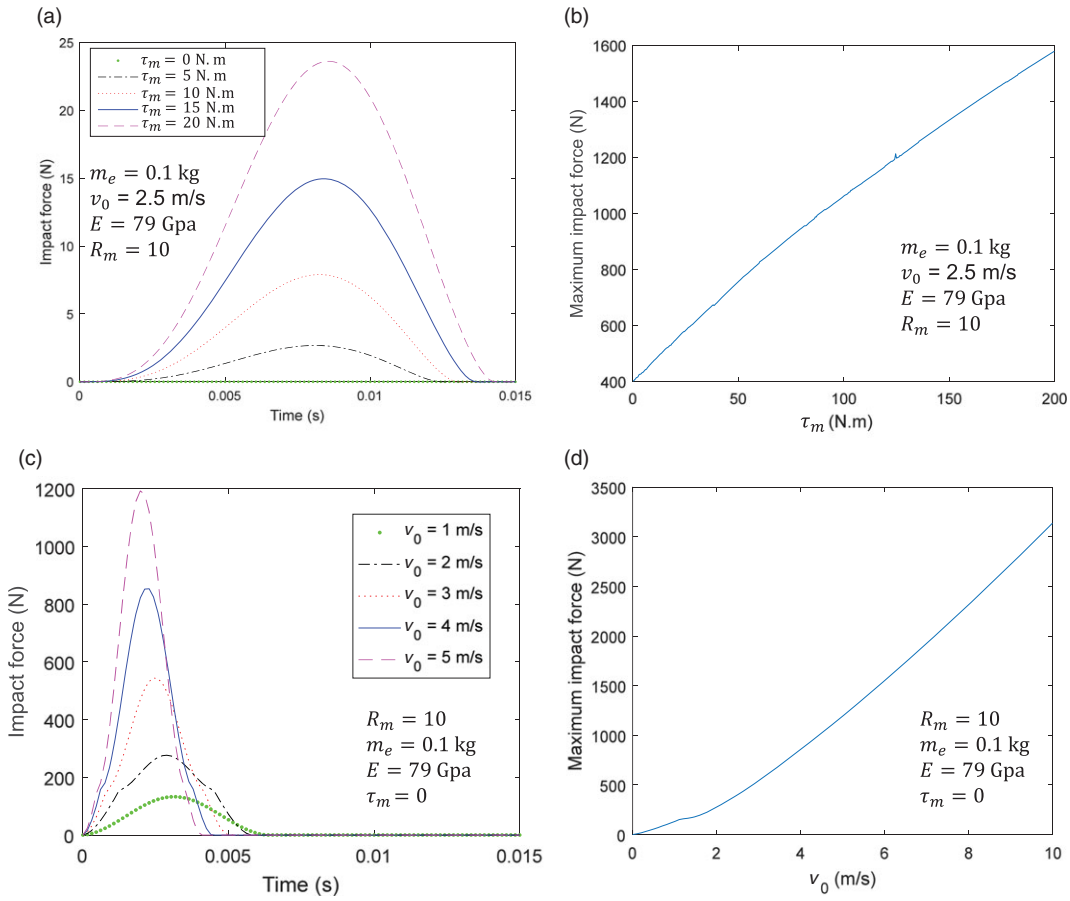


Fig. 9. Parameters effects on the impact force of the CL design. (a) The impact force versus time given various motor torque, (b) the maximum impact force versus motor torque, (c) the impact force versus time given various impact velocities, and (d) the maximum impact force versus impact velocity.

1. The time stamp of the peak impact force shifts right along with the increasing of k_l, R_m, or m_e.
2. Both the peak value and the duration of the impact force increase along with the increasing of R_m or m_e.
3. The profile of $F_{\max}$ versus k_l is close to a sigmoid function. In other words, $F_{\max}$ has a sharp "step" change given a certain range of lateral stiffness variation but it is saturated at both sides. This indicates that it is critical to find the sensitive interval of lateral stiffness variation in order to effectively reduce impact force.
4. The profile of $F_{\max}$ versus m_e is highly nonlinear. $F_{\max}$ dramatically grows when m_e increases from a small value and gradually becomes saturated when m_e increases large enough.

It is observed that the solid blue line in Fig. 8(a) is different in shape from the other curves. We do not have clear clues to explain this particular case. One potential reason could be the different physical properties of the contact objects (bones, skins, robots, and the covering material). When the impact force is relatively small, it is mainly affected by the physical properties of the surface materials (the skins and the covering). When the impact force is sufficiently large, it is mainly affected by the physical properties of the inner materials (the bones and the robots). When the impact force in the intermediary range (which could correspond to the case with the solid blue line), the impact force is affected by the combinations of these four materials, which could result in different impact force profiles.

5.1.2. Effect of actuation parameters on the impact force. Now let us study the effects of the actuation parameters (τ_m and v_0) on the impact force. Figure 9(a) and (b) show the effects of τ_m on

https://doi.org/10.1017/S0263574720001472 Published online by Cambridge University Press

the impact force, and Fig. 9(c) and (d) show how does the impact velocity affects the impact force. Observations from this figure are listed below:

1. While $F_{\max}$ monotonically increases along with the increasing of τ_m and v_0, its nonlinearity is not significant.
2. The impact duration of the impact force is barely affected by τ_m, but it decreases along with the increase in v_0.
3. The instant of peak impact force is barely affected by τ_m, but it shifts left along with the increase in v_0.

We explored the general effects of the design parameters of k_l, R_m, and m_e and actuation parameters of τ_m and v_0 on the impact force of the pHRI system with the CL design. All of these parameters have prominent effects on $F_{\max}$, from which v_0 and m_e may be the ones that affect $F_{\max}$ most substantially.

One of the most important findings is that $F_{\max}$ monotonically increases only in a certain range of k_l. Outside of this range, tuning stiffness is effective for reducing maximum impact force. Since we are interested in reducing the impact force with the CL design with variable stiffness, we will further study how varying stiffness affects the reduction of maximum impact force for the CL design in the following section.

5.2. Effects of variable stiffness on the reduction of the maximum impact force

We have discussed the general effects of the design parameters (k_l, R_m, and m_e) and actuation parameters (τ_m and v_0) on the impact force in the last section. In this section, we further discuss the effect of the lateral stiffness (k_l) on the impact force, since we are particularly interested in leveraging variable stiffness designs to address safety issues for pHRIs. Please note, we consider a robotic link whose stiffness is continuously adjustable in the following discussions. Since we consider the CL design with variable stiffness, the maximum impact force $F_{\max}$ is actually a function of the lateral stiffness k_l. We evaluate effects of various design and actuation parameters on the reduction of $F_{\max}(k_l)$ over a reasonable range of variable stiffness, $k_l \in [k_{l\min}, k_{l\max}]$. Here, the term "reasonable" means that the stiffness can be realized in hardware with appropriate materials and/or geometries.

5.2.1. Evaluation metrics. To evaluate the reduction of the maximum impact force, we consider three quantitative metrics: (1) the reduction ratio, (2) the reduction rate, and (3) the critical lateral stiffness corresponding to the maximum reduction rate. We describe each in the following.

First, it is desired to have a large reduction of maximum impact force $F_{\max}$ for a reasonable range of stiffness variation. In other words, we want to reduce $F_{\max}$ as much as possible via reducing the mechanical stiffness. We define the reduction ratio of the maximum impact force R_f by:

$$R_f = \frac{\max(F_{\max}(k_l)) - \min(F_{\max}(k_l))}{\min(F_{\max}(k_l))} \times 100\%, \quad k_l \in [k_{l\min}, k_{l\max}] \tag{7}$$

where k_l is in a reasonable range that is feasible in hardware.

Second, we also seek a rapidly changing rate of the maximum impact force in response to a stiffness change. This metric can be quantified as the maximum reduction rate of the maximum impact force, mathematically defined by:

$$D_{\max} = \max(D(k_l)), \quad k_l \in [k_{l\min}, k_{l\max}] \tag{8}$$

where $D(k_l) = F'_{\max}(k_l)$ is the changing rate the maximum impact force with respect to the lateral stiffness. The unit of $D(k_l)$ is m (i.e., $N/(N/m) = m$). Essentially, we seek for a CL design with a large $D_{\max}$.

Third, the absolute value of k_l should also be considered as it determines the base of link stiffness which further determines the material choice and geometric design. More specifically, we design the

https://doi.org/10.1017/S0263574720001472 Published online by Cambridge University Press

Table III. Metrics for evaluating effects of variable stiffness on reduction of the maximum impact force.

Symbol	Description	Definition
R_f	Reduction ratio of the maximum impact force	$R_f = \frac{\max(F_{\max}(k_l)) - \min(F_{\max}(k_l))}{\min(F_{\max}(k_l))} \times 100\%$, $k_l \in [k_{l\min}, k_{l\max}]$
$D(k_l)$	Reduction rate of the maximum impact force	$D(k_l) = F'_{\max}(k_l)$, $D_{\max} = \max(D(k_l))$, $k_l \in [k_{l\min}, k_{l\max}]$
K_c	Critical lateral stiffness corresponding to the maximum reduction rate	$K_c = k_l^* := \{k_l \mid D(k_l) = D_{\max}, k_l \in [k_{l\min}, k_{l\max}]\}$

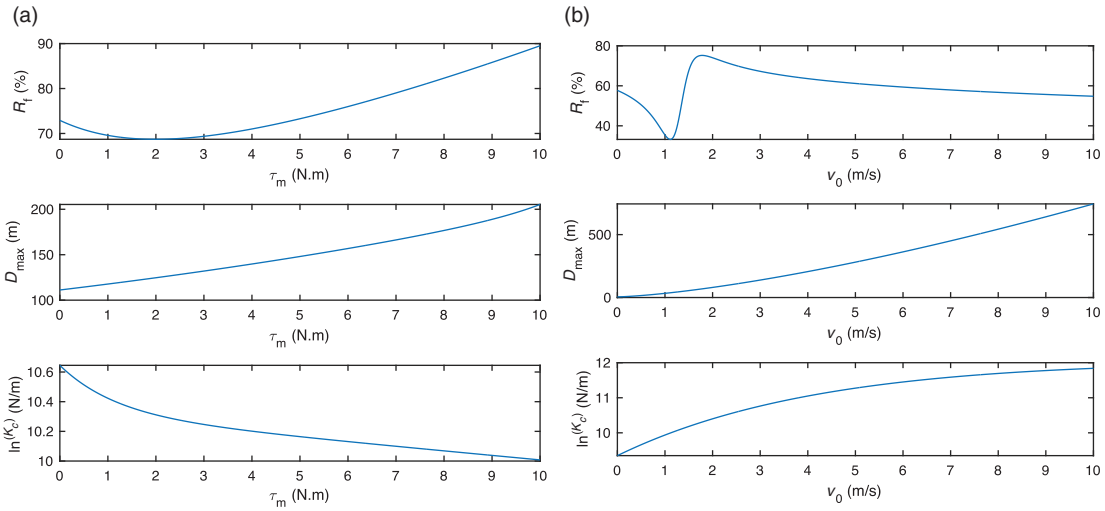


Fig. 10. (a) The effects of τ_m on the proposed criteria given $v_0 = 2.5$ m/s, $R_m = 10$, and $m_e = 0.1$ kg, and variable stiffness, (b) the effects of v_0 on the proposed criteria given $\tau_m = 0$ N.m, $R_m = 10$, and $m_e = 0.1$ kg, and variable stiffness.

link stiffness near the so-called critical stiffness which corresponds to the maximum derivative $D_{\max}$, mathematically written as:

$$K_c = k_l^* := \{k_l \mid D(k_l) = D_{\max}, \quad k_l \in [k_{l\min}, k_{l\max}]\} \tag{9}$$

The symbol, description, and definition of the aforementioned evaluation metrics are summarized in Table III for the sake of clarity.

It is worth mentioning that the aforementioned three evaluation metrics are used to evaluate the effect of the variable stiffness instead of the impact outcome. We assume the maximum impact force $F_{\max}$ from the system modeling is equal to the upper bound of the impact force that can be tolerated by humans.

5.2.2. Evaluation results. To develop a useful design guideline, we study effects of various parameters such as τ_m, v_0, R_m, and m_e on the three aforementioned design criteria R_f, $D_{\max}$, and K_c. Here, we first take a natural logarithm operation of the actual lateral stiffnes and then we export the results (k_l) to Eqs. (7), (8), and (9) for the sake of consistency.

Figure 10(a) shows the effects of τ_m on the three evaluation metrix R_f, $D_{\max}$, and K_c for variable stiffness. Along with the increasing of the motor torque τ_m, R_f slightly decreases first and then monotonically increases, and R_f is more than 70% given these parameters which is promising for the safety purpose of pHRI. $D_{\max}$ monotonically increases while K_c continuously decreases with the increasing of the motor torque τ_m. The figure shows that a larger motor torque τ_m can result in a large $D_{\max}$ but a small K_c.

Figure 10(b) shows the effects of the impact velocity v_0 on the design criteria. It is observed that R_f has a local minimum and a local maximum and converges to a constant along with the growth of the impact velocity v_0. Both $D_{\max}$ and K_c have a trend of monotonically increasing along with the growth of the impact velocity v_0.

https://doi.org/10.1017/S0263574720001472 Published online by Cambridge University Press

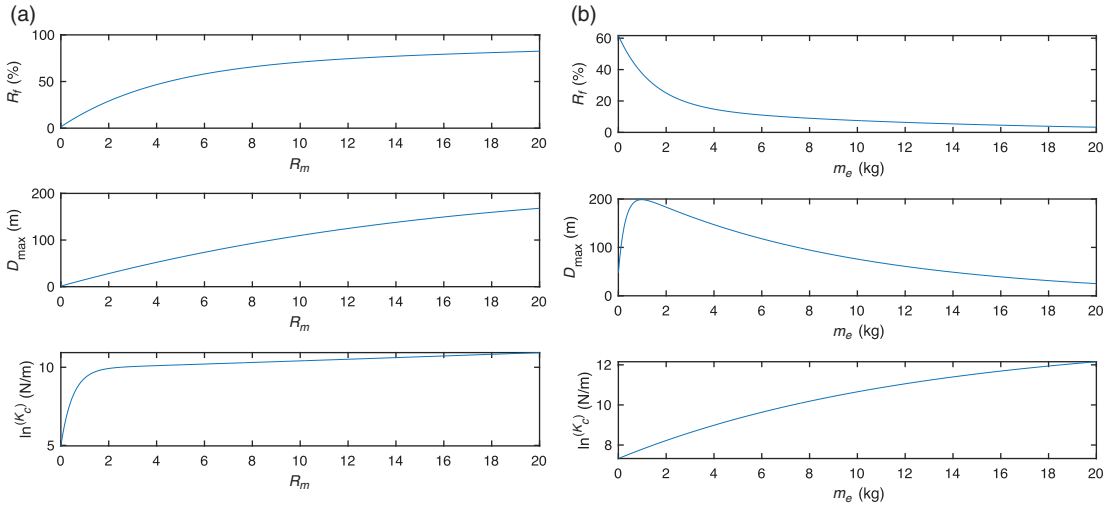


Fig. 11. (a) The effects of R_m on the proposed criteria given $\tau_m = 0$ N.m, $v_0 = 2.5$ m/s, $m_e = 0.1$ kg, and variable stiffness, (b) the effects of m_e on the proposed criteria given $\tau_m = 0$ N.m, $v_0 = 2.5$ m/s, $R_m m = 10$, and variable stiffness.

Figure 11(a) shows the effects of R_m on the design criteria under variable stiffness. It is observed that R_f and $D_{\max}$ have a trend of monotonically increasing with the growth of R_m. The critical stiffness K_c is affected by small R_m, and K_c is saturated with the growth of R_m. From the perspective of design, one may prefer a large R_m to obtain a large R_f and $D_{\max}$.

Figure 11(b) shows the effects of m_e on the proposed three design criteria. It is observed that R_f monotonically decreases along with the increasing of m_e, and the trend is dramatic when m_e is small and gradually converges to a constant. $D_{\max}$ first rapidly increases and reaches a local maximum then slowly decreases along with the increasing of m_e and converges to a constant as well. The critical stiffness K_c monotonically increases along with the growth of m_e and converges to a constant. These observations indicate that m_e may only significantly affect the design criteria when m_e is small.

6. Design Guidelines

With the parametric studies presented above, one may be able to summarize the guidelines for designing VSLs for safe pHRI. Recall the actuation parameters include $\{\tau_m, v_0\}$ and the design parameters include $\{R_m, m_e, k_l\}$. The key findings are listed as the following:

1. Both the actuation and design parameters affect $F_{\max}$, from which v_0 and m_e may be the ones that affect $F_{\max}$ most significantly. Although m_e considerably affects $F_{\max}$ when m_e is small (around 5 kg as shown in Fig. 9(f)), this effect gradually decreases as m_e increases.
2. Both the actuation and design parameters affect the three design criteria, from which the design parameters R_m and m_e substantially affect R_f while the actuation parameters v_0 and τ_m do not.
3. To achieve a significant impact force reduction, the range of k_l should be designed/selected to cover the sharp reduction range of the sigmoid function, as shown in Fig. 8(b) and this is the most important guideline to design the relative variation of the lateral stiffness. The absolute value of the lateral stiffness should be calculated by Eq. (9), which is determined by material properties and geometric dimensions of the robot link.
4. m_e have prominent effects on R_f, $D_{\max}$, and K_c when $m_e \subseteq [0, 2]$ kg, and the effects gradually decrease when $m_e > 2$ kg. A small m_e gives a large R_f and small K_c, which leads to the ideal design for safe human–robot interaction.
5. R_m significantly affects R_f and $D_{\max}$ when $R_m \subseteq [0, 10]$, and the effects gradually decrease when $R_m > 10$. A large R_m leads a large R_f and $D_{\max}$ which is desired for safe physical interaction.

To design a variable stiffness CL for safe pHRI, we propose the following process, as shown in Fig. 12. First, we specify link design independent parameters, including neck, head, and motor

https://doi.org/10.1017/S0263574720001472 Published online by Cambridge University Press

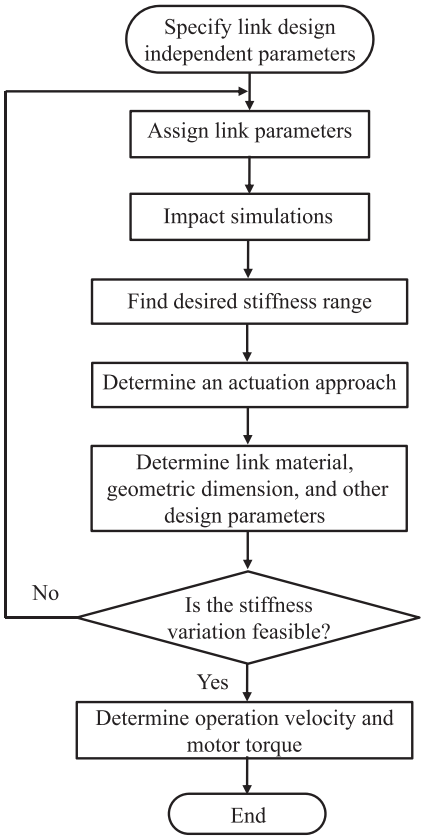


Fig. 12. The flowchart for designing a variable stiffness link for safe pHRI.

parameters. These parameters will be constant for all impact dynamics simulations. Second, we assume realistic values for the robotic link parameters such as link mass m_r and link length L but not including the lateral stiffness k_l. These link parameters may need to be changed if a feasible design is not available. Third, we determine the desired range and relative variation of the stiffness by executing a series of impact simulations with an acceptable impact force threshold $F_{\max}$ and maximum impact velocity v_0 as the inputs. Fourth, once the stiffness range is determined, we implement a practical actuation approach (e.g., morphing beams, rotating beam, changing effective length, layer jamming, etc.) for achieving the range of variable stiffness previously determined. Fifth, we choose the appropriate material, geometric dimensions (e.g., w, h for the cross-section), and finalize other design parameters (e.g., mass ratio R_m and end effector mass m_e). If the range of stiffness variation turns out to be infeasible in practice, one has to modify non-stiffness parameters, and the whole procedure has to be iterated until a feasible solution is obtained. Once a feasible design is obtained, one can then determine the maximum operating speed of the robot and the motor torque by executing more impact simulations with varying impact velocity and motor torque and ensuring the maximum impact force is below the acceptable threshold.

It is worth noting that in this study, we assume that the studied pHRI system has an active (rather than passive) compliance, that is, the robot stiffness (hence the bandwidth) is controllable. Although the proposed strategy may work for the task of off-line motion planning tasks, it may be challenging to apply for tasks with online motion planning unless high bandwidth of stiffness tuning mechanisms is available. Although introducing more powerful actuators could potentially increase the bandwidth, it usually comes with larger inertia (hence larger impact force), which is not desired in this study.

7. A Case Study

With the design guidelines summarized above, we presented as a simulation case study of the CL with variable stiffness for safety pHRI in this section.

https://doi.org/10.1017/S0263574720001472 Published online by Cambridge University Press

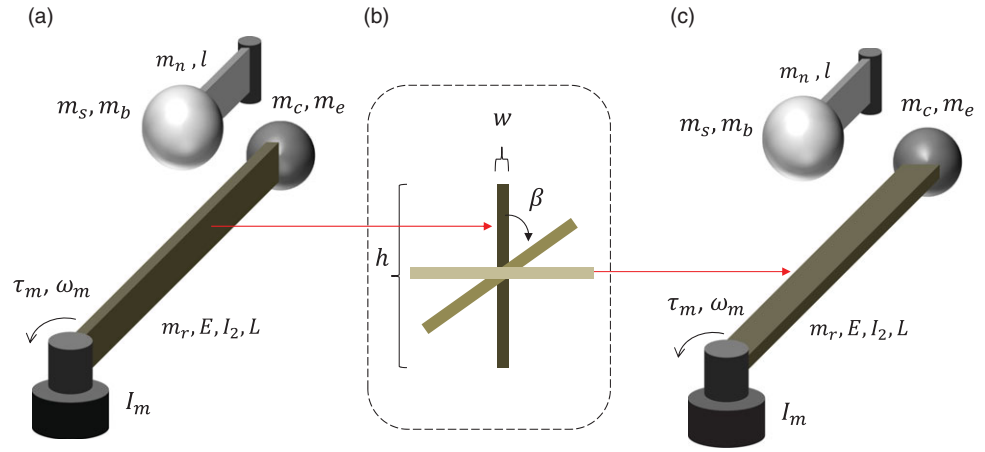


Fig. 13. The proposed variable stiffness link. (a) vertical configuration of the robot link (compliant mode), (b) the cross section of the link given a rotation angle, (c) horizontal configuration of the robot link (stiff mode).

7.1. Design procedure

First, we specify the independent parameters for the pHRI system. These parameters are realistic, and they are fixed based on the experiment setup. Second, we assign realistic link parameters. These link parameters are temporarily assigned to run the impact simulation and are subject to change and iterate depending on the following analysis. Third, we run the impact simulation with a sweeping of the lateral stiffness, and one may find that the maximum impact force profile is close to Fig. 8(b). In this case, k_l can be temperately specified as $k_{l\,\min} = e^5$ N/m and $k_{l\,\max} = e^{12}$ N/m in order to cover the sharp reduction range of the sigmoid function in order to obtain a decent R_f. Remember, e is the base of the natural logarithm.

Fourth, we now start to design an approach to achieve the variable stiffness. We use a cantilever beam that is able to rotate around its axis, as shown in Fig. 13. Specifically, the cantilever beam is installed on a motor hub with a payload at the tip. Assume the cross section of the link is rectangular, and its height of h is significantly larger than its width of w. Assume the rotation angle is β, as shown in Fig. 13(b), and the beam can be locked on the motor hub after any rotation angle. The lateral stiffness of the link varies depending on the rotation angle of β. Two ultimate cases of the minimal and maximum lateral stiffness are located at $\beta = 0°$ and $\beta = 90°$, as shown with the compliant and stiff mode in Fig. 13(a) and (c), respectively. The maximum ratio of the lateral stiffness can be calculated as:

$$R_k = \frac{w^2}{h^2} \tag{10}$$

Fifth, with this specific design in mind, we can determine the link material and finalize its geometric dimensions as well as other design parameters. A customized aluminum beam (71 GPa) may be able to achieve the stiffness requirement. We found that an aluminum beam with $w = 2$ mm, $h = 50$ mm, and $L = 400$ mm will result in $k_{l\,\min} = e^{4.71}$ N/m and $k_{l\,\max} = e^{11.74}$ (N/m) as shown in Fig. 13(a)–(c), respectively, which is able to cover the sharp reduction range of the sigmoid function.

Meanwhile, we would like to determine other design parameters R_m and m_e. Based on the geometric parameters specified above, the mass of the link is calculated as $m_r = 100$ g. As we discussed previously, a large R_m and a small m_e would be preferred to achieve a large R_f and $D_{\max}$. Here, $R_m = 10$ would be a good candidate to have a descent performance and then we will select $m_e = 10$ g for this case study.

Finally, since the proposed rotating cantilever beam is feasible for the variable stiffness, we can specify the actuation parameters of τ_m and v_0. According to the findings in Section 6, both the actuation parameters v_0 and τ_m affect the $F_{\max}$ but v_0 has more significant effects on $F_{\max}$. In addition, neither v_0 nor τ_m affect R_f, $D_{\max}$, and K_c significantly. Therefore, in this study, we simply set $\tau_m = 0$ N.m and explore the range of v_0 such that $F_{\max}$ could satisfy the safety requirement. We consider that $F_{\max} = 500$ N is a safety criterion, and we tried a few different v_0 as shown in Fig. 14 and found the

https://doi.org/10.1017/S0263574720001472 Published online by Cambridge University Press

Table IV. Design and actuation parameters of the pHRI system for the simulation case study.

Parameters (units)	Symbol	Value
Beam rotation angle (°)	β	[0,90]
Beam Young's modulus (N/m^2)	E_b	71E9
Beam width (m)	w	2E-3
Beam height (m)	h	50E-3
Beam length (m)	L	400E-3
Beam variable stiffness (N/m)	k_l	[$e^{4.71}$, $e^{11.74}$]
Beam mass (kg)	m_r	0.1
End effector mass (kg)	m_e	0.01
Mass ratio	R_m	10
Motor torque (N.m)	τ_m	0
Impact velocity (m/s)	v_0	[2.1, 2.85]

rough value of the maximum safe v_0 may be near 2.5 m/s. Remember, we take a natural logarithm operation of the actual lateral stiffnes in the x-axis in Fig. 14 in order to see a clear trend of the stiffness variation. Next, we will elaborate the impact velocity depending on the robot's operation task.

Consider the robot link carries a load from one position to another. For accuracy and efficiency purposes, it may operate in three phases with a speed of low-high-low. The operation velocity starts from 0 and is accelerated to high speed for a minimal time in the first phase, and the robot operates with the maximum safe speed in the second phase and then slows down when it approaches the destination and finally stops there at the end of the third phase.

In terms of the robot link stiffness, high stiffnesses may be required in the initial and final phase to overcome the inertia from the acceleration or deceleration. In addition, force control or position control may be applied to the initial or final phase, which requires a high stiffness of the robot arm. In contrast, the robot could be operated with low stiffness during the middle phase to ensure safety. Consider this particular design with the impact force of 500 N as the impact tolerance. The robot may start from and end up with the configuration in Fig. 13(c) with the stiff mode, and the maximum operation speed may be less than 2.1 m/s to ensure safety according to Fig. 14. In the middle phase, the robot link changes its configuration to Fig. 13(a) with its compliant mode, and the operation speed can be up to 2.85 m/s and ensure safety meanwhile according to Fig. 14. However, if the stiffness of the robot link is fixed and not able to change, the maximum operating speed of the robot during the entire operation would be 2.1 m/s to ensure safety. Table IV summarizes the design and actuation parameters of the pHRI system for the simulation case study.

7.2. Design evaluation

It is observed that the proposed design can cause significant reduction of $F_{\max}$. Specifically, the VSL can achieve R_f = 68% and $D_{\max}$ = 120 m, given the stiffness variations from configuration Fig. 13(c)–(a) at a specific speed of v_0 = 2.85 m/s. In addition, the VSL increased the maximal safety operation speed by 35%, which can significantly improve the robot's working efficiency.

8. Discussion

It is worth noting that this work does not evaluate the effect of the torsional compliance considering the physical prototypes and setups implemented in this study. But one may pay attention to the torsional stiffness, in addition to the lateral stiffness, if the torsional compliance is comparable with the lateral compliance in magnitude[44] or torsional moments are created by the impact force with an offset.

The concept of the variable stiffness arm works for the tasks of offline motion planning.[35] It may be challenging to apply for tasks of online motion planning unless high bandwidth of stiffness tuning mechanisms is available. Although introducing more powerful actuators could potentially increase the bandwidth, it usually comes with larger inertia (hence larger impact force), which is not desired in this study.

The Hertz contact model applied in this work does not consider friction on the contact surfaces. Contact problems with friction are usually very complicated because the contact surfaces could have

https://doi.org/10.1017/S0263574720001472 Published online by Cambridge University Press

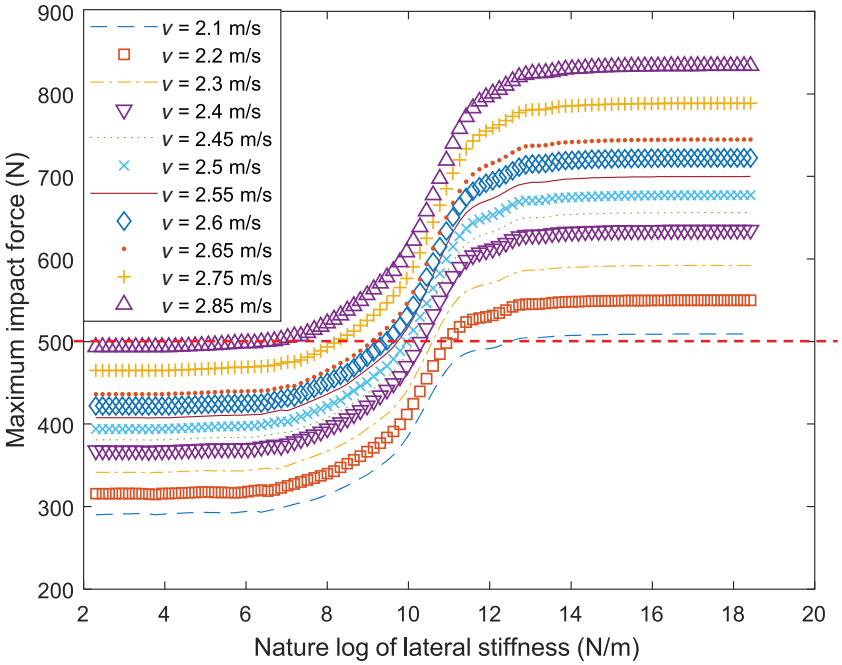


Fig. 14. Exploration of the maximum and safe operation velocity for the proposed robot link.

slipping, sliding, rolling, or tension release determined by the normal and tangential stresses on the contact surface.[46,47] This study focuses on the parametric study of CL design for safe pHRI, so we hold the frictionless assumption and does not investigate the friction effect for simplicity. In fact, the impact surfaces may have frictions in the real world, which could cause partial slip between dissimilar solids,[48] and may further cause injuries such as lacerations due to the tangential friction force.[45]

This work explores how the design and actuation parameters affect the impact force of pHRI systems, which include robotic dynamics, impact model, and head dynamics. The model developed in this study is parametric and intends to discover trends that generally guide mechanical design. Here, we consider a simplified case for the sake of convenient analysis. The robotic system includes a rigid joint and a CL. For complex robotic systems with multiple joints and flexible links, one may also refer to the methods presented in this paper. Note, the robot pose will also play a significant role in determining the maximum impact force when it comes to the multi-linked robotic system.

9. Conclusions

This work conducts a parametric study of the CL design for safe pHRI. The study explores the effects of design and actuation parameters on the impact force, and one of the most important findings is that the maximum impact force has a sharp "step" change given a certain range of lateral stiffness variation, but it is saturated from both sides, behaving like a sigmoid function. Therefore, to achieve a significant impact force reduction, the range of link stiffness of a VSL should be designed/selected to cover the sharp reduction range of the sigmoid function, which can be determined by material properties and geometric dimensions of the robot link. We further derive a list of concrete guidelines and processes for designing variable stiffness robotic links based on the simulations. To validate the design guidelines and procedures, we conducted a simulation case study in which a rotating beam design is utilized for achieving the variable stiffness. The results show that the CL design successfully achieves the maximum impact force reduction of 68% with the maximum safety operation speeds improvement of 35%. We conclude that the CL design can be used as a promising alternative solution to address the safety constraints in pHRI. It is worth noting that the robot in the pHRI system is considered as a single CL and rigid joint in this work, and future work includes exploring the scenarios that the robot has multiple CLs.

https://doi.org/10.1017/S0263574720001472 Published online by Cambridge University Press

Acknowledgment
This material is based on work supported by the National Science Foundation under Grant No: CMMI-1637656. Any opinions, findings, and conclusions or recommendations expressed in this material are those of the author(s) and do not necessarily reflect the views of the funding agencies.

Conflicts of Interest
The authors declare none.

References

1. J. Versace, A Review of the Severity Index, *SAE Technical Paper 710881* (1971).
2. D. Gao and C. W. Wampler, "Head injury criterion," *IEEE Robot. Autom. Mag.* **16**(4), 71–74 (2009).
3. S. Haddadin, A. Albu-Schäffer and G. Hirzinger, "Requirements for safe robots: Measurements, analysis and new insights," *Int. J. Rob. Res.* **28**(11), 1507–1527 (2009).
4. ISO10218-1:2006, *Robots for Industrial Environments - Safety Requirements. Part I: Robot* (International Organization for Standarization, 2006).
5. S. Haddadin, A. Albu-Schäffer, M. Frommberger, J. Rossmann and G. Hirzinger, "The 'DLR Crash Report': Towards a Standard Crash-Testing Protocol for Robot Safety-Part I: Results," *Proceedings of the IEEE International Conference on Robotics and Automation* (2009) pp. 272–279.
6. J. Melvin, Human Tolerance to Impact Conditions as Related to Motor Vehicle Design, *SAE Report J885* (1980).
7. B. Vanderborght, etc., "Variable impedance actuators: A review," *Rob. Auton. Syst.* **61**(12), 1601–1614 (2013).
8. A. Albu-Schäffer, S. Haddadin, C. Ott, A. Stemmer, T. Wimböck and G. Hirzinger, "The DLR lightweight robot: Design and control concepts for robots in human environments," *Ind. Rob.* **34**(5), 376–385 (2007).
9. F. Ficuciello, L. Villani and B. Siciliano, "Variable impedance control of redundant manipulators for intuitive human–robot physical interaction," *IEEE Trans. Robot.* **31**(4), 850–863 (2015).
10. M. Laffranchi, N. G. Tsagarakis and D. G. Caldwell, "Analysis and development of a semiactive damper for compliant actuation systems," *IEEE ASME Trans. Mechatron.* **18**(2), 744–753 (2013).
11. P. Fauteux, M. Lauria, B. Heintz and F. Michaud, "Dual-differential rheological actuator for high-performance physical robotic interaction," *IEEE Trans. Robot.* **26**(4), 607–618 (2010).
12. H. A. Sodano, J. S. Bae, D. J. Inman and W. K. Belvin, "Improved concept and model of eddy current damper," *J. Vib. Acoust.* **128**(3), 294–302 (2006).
13. C. Y. Hou, "Fluid dynamics and behavior of nonlinear viscous fluid dampers," *J. Struct. Eng.* **134**(1), 56–63 (2008).
14. G. A. Pratt and M. M. Williamson, "Series Elastic Actuators," *Proceedings of the IEEE International Conference on Intelligent Robots and Systems* (1995) pp. 399–406.
15. A. Bicchi, G. Tonietti and E. Piaggio, "Design, Realization and Control of Soft Robot Arms for Intrinsically Safe Interaction with Humans," *IARP/RAS Workshop on Technical Challenges for Dependable Robots in Human Environments* (2002) pp. 79–87.
16. A. Bicchi, etc, "Physical Human-Robot Interaction: Dependability, Safety, and Performance," *The 10th IEEE International Workshop on Advanced Motion Control* (2008) pp. 9–14.
17. A. Bicchi and G. Tonietti, "Fast and 'soft-arm' tactics [robot arm design]," *IEEE Robot. Autom. Mag.* **11**(2), 22–33 (2004).
18. G. Tonietti, R. Schiavi and A. Bicchi, "Design and Control of a Variable Stiffness Actuator for Safe and Fast Physical Human Robot Interaction," *Proceedings of the IEEE International Conference on Robotics and Automation* (2005) pp. 526–531.
19. R. Schiavi, G. Grioli, S. Sen and A. Bicchi, "VSA-II: A Novel Prototype of Variable Stiffness Actuator for Safe and Performing Robots Interacting with Humans," *Proceedings of the IEEE International Conference on Robotics and Automation* (2008) pp. 2171–2176.
20. S. Wolf and G. Hirzinger, "A New Variable Stiffness Design: Matching Requirements of the Next Robot Generation," *Proceedings of the IEEE International Conference on Robotics and Automation* (2008) pp. 1741–1746.
21. S. Wolf, O. Eiberger and G. Hirzinger, "The DLR FSJ: Energy Based Design of a Variable Stiffness Joint," *Proceedings of the IEEE International Conference on Robotics and Automation* (2011) pp. 5082–5089.
22. W. Friedl, H. Höppner, F. Petit and G. Hirzinger, "Wrist and Forearm Rotation of the DLR Hand Arm System: Mechanical Design, Shape Analysis and Experimental Validation," *Proceedings of the IEEE International Conference on Intelligent Robots and Systems* (2011) pp. 1836–1842.
23. M. Zinn, B. Roth, O. Khatib and J. K. Salisbury, "A new actuation approach for human friendly robot design," *Int. J. Rob. Res.* **23**(4–5), 379–398 (2004).
24. l. Chen, M. Garabini, M. Laffranchi, N. Kashiri, N. G. Tsagarakis, A. Bicchi and D. G. Caldwell, "Optimal Control for Maximizing Velocity of the CompAct™ Compliant Actuator," *Proceedings of the IEEE International Conference on Robotics and Automation* (2013) pp. 516–522.
25. S. Haddadin, A. Albu-Schäffer, O. Eiberger and G. Hirzinger, "New Insights Concerning Intrinsic Joint Elasticity for Safety," *Proceedings of the IEEE International Conference on Intelligent Robots and Systems* (2010) pp. 2181–2187.

https://doi.org/10.1017/S0263574720001472 Published online by Cambridge University Press

26. N. D. Vuong, R. Li, C. M. Chew, A. Jafari and J. Polden, "A novel variable stiffness mechanism with linear spring characteristic for machining operations," *Robotica* **35**(7), 1627–1637 (2017).
27. W. Wang, X. Fu, Y. Li and C. Yun, "Design and implementation of a variable stiffness actuator based on flexible gear rack mechanism," *Robotica* **36**(3), 448–462 (2018).
28. K. C. Galloway, J. E. Clark and D. E. Koditschek, "Variable stiffness legs for robust, efficient, and stable dynamic running," *J. Mech. Robot.* **5**(1), 011009 (2013).
29. Y. J. Kim, S. Cheng, S. Kim and K. Iagnemma, "A novel layer jamming mechanism with tunable stiffness capability for minimally invasive surgery," *IEEE Trans. Robot.* **29**(4), 1031–1042 (2013).
30. L. Hines, V. Arabagi and M. Sitti, "Shape memory polymer-based flexure stiffness control in a miniature flapping-wing robot," *IEEE Trans. Robot.* **28**(4), 987–990 (2012).
31. J. J. Park, B. S. Kim, J. B. Song and H. S. Kim, "Safe Link Mechanism Based on Passive Compliance for Safe Human-Robot Collision," *Proceedings of the IEEE International Conference on Robotics and Automation* (2007) pp. 1152–1157.
32. J. J. Park, B. S. Kim, J. B. Song and H. S. Kim, "Safe link mechanism based on nonlinear stiffness for collision safety," *Mech. Mach. Theory* **43**(10), 1332–1348 (2008).
33. M. Zhang, T. Laliberté and C. Gosselin, "Force capabilities of two-degree-of-freedom serial robots equipped with passive isotropic force limiters," *J. Mech. Robot.* **8**(5), 051002 (2016).
34. Y. She, H. J. Su, C. Lai and D. Meng, "Design and Prototype of a Tunable Stiffness Arm for Safe Human-Robot Interaction," *ASME International Design Engineering Technical Conferences and Computers and Information in Engineering Conference* (2016) pp. V05BT07A063.
35. Y. She, H. J. Su, C. Lai and D. Meng, "Design and modeling of a continuously tunable stiffness arm for safe physical human–robot interaction," *J. Mech. Robot.* **12**(1), 011006 (2020).
36. A. Stilli, H. A. Wurdemann and K. Althoefer, "Shrinkable, Stiffness-Controllable Soft Manipulator Based on a Bio-Inspired Antagonistic Actuation Principle," *Proceedings of the IEEE International Conference on Intelligent Robots and Systems* (2014) pp. 2476–2481.
37. A. Stilli, H. A. Wurdemann and K. Althoefer, "A novel concept for safe, stiffness-controllable robot links," *Soft Robot.* **4**(1), 16–22 (2017).
38. Y. She, H. J. Su and C. J. Hurd, "Shape Optimization of 2D Compliant Links for Design of Inherently Safe Robots," *ASME International Design Engineering Technical Conferences and Computers and Information in Engineering Conference* (2015) pp. V05BT08A004.
39. Y. She, H. J. Su, D. Meng, S. Song and J. Wang, "Design and modeling of a compliant link for inherently safe corobots," *J. Mech. Robot.* **10**(1), 011001 (2018).
40. H. Hertz, "On the contact on elastic solids," *J. Math.* **92**, 156–171 (1881). (in German); also in: Miscellaneous Papers (in English), Macmillan, London (1896).
41. J. J. Park, S. Haddadin, J. B. Song and A. Albu-Schäffer, "Designing Optimally Safe Robot Surface Properties for Minimizing the Stress Characteristics of Human-Robot Collisions," *Proceedings of the IEEE International Conference on Robotics and Automation* (2011) pp. 5413–5420.
42. I. P. Herman, *Physics of the Human Body* (Springer, New York, 2016).
43. Y. She, Compliant Robotic Arms for Inherently Safe Physical Human-Robot Interaction *Ph.D. Thesis* (The Ohio State University, New York City, 2018).
44. G. Chen and L. Howell, "Two general solutions of torsional compliance for variable rectangular cross-section hinges in compliant mechanisms," *Precis. Eng.* **33**(3), 268–274 (2009).
45. N. Lauzier and C. Gosselin, "A comparison of the effectiveness of design approaches for human-friendly robots," *J. Mech. Des.* **137**(8), 082302 (2015).
46. M. Machado, P. Moreira, P. Flores and H. M. Lankarani, "Compliant contact force models in multibody dynamics: Evolution of the Hertz contact theory," *Mech. Mach. Theory* **53**, 99–121 (2012).
47. N. Chandrasekaran, W. E. Haisler and R. E. Goforth, "Finite element analysis of Hertz contact problem with friction," *Finite Elem. Anal. Des.* **3**(1), 39–56 (1987).
48. B. Storakers and D. Elaguine, "Hertz contact at finite friction and arbitrary profiles," *J. Mech. Phys. Solids* **53**(6), 1422–1447 (2005).
49. W. J. Book, "Recursive Lagrangian dynamics of flexible manipulator arms," *Int. J. Rob. Res.* **3**(3), 87–100 (1984).
50. S. Cetinkunt and W. J. Book, "Symbolic modeling and dynamic simulation of robotic manipulators with compliant links and joints," *Robot. Comput. Integr. Manuf.* **5**(4), 301–310 (1989).
51. M. Moallem, R. V. Patel and K. Khorasani, "An inverse dynamics control strategy for tip position tracking of flexible multi–link manipulators," *J. Robot. Syst.* **14**(9), 649–658 (1997).
52. G. P. Cai and C. W. Lim, "Dynamics studies of a flexible hub–beam system with significant damping effect," *J. Sound Vib.* **318**(1–2), 1–17 (2008).
53. P. Reddy, K. V. Shihabudheen and J. Jacob, "Precise non linear modeling of flexible link flexible joint manipulator," *Int. Review Model. Sim.* **5**(3B), 1368–1374 (2012).
54. S. Song, Y. She, J. Wang and H. Su, "Toward tradeoff between impact force reduction and maximum safe speed: Dynamic parameter optimization of variable stiffness robots," *J. Mech. Robot.* **12**(5), 054503–054511 (2020).

https://doi.org/10.1017/S0263574720001472 Published online by Cambridge University Press